



# Calcium and titanium isotope fractionation in refractory inclusions: Tracers of condensation and inheritance in the early solar protoplanetary disk



J.I. Simon <sup>a,\*</sup>, M.K. Jordan <sup>b</sup>, M.J. Tappa <sup>a,1</sup>, E.A. Schauble <sup>b</sup>, I.E. Kohl <sup>b</sup>, E.D. Young <sup>b</sup>

<sup>a</sup> Center for Isotope Cosmochemistry & Geochronology, Astromaterials Research and Exploration Science Division, NASA-Johnson Space Center, Houston, TX, USA

<sup>b</sup> Department of Earth, Planetary, and Space Sciences, UCLA, Los Angeles, CA, USA

## ARTICLE INFO

### Article history:

Received 26 January 2017

Received in revised form 1 May 2017

Accepted 3 May 2017

Editor: F. Moynier

### Keywords:

condensation

Ca-, Al-rich inclusions

Ca and Ti isotope fractionation

solar nebula

protoplanetary disk

<sup>50</sup>Ti isotopic anomalies

## ABSTRACT

Measured and modeled Ca and Ti isotopic fractionation effects in a diverse suite of refractory inclusions are used to understand processes of condensation in the solar protoplanetary disk where they and their precursor materials formed. This coordinated approach reveals largely decoupled isotopic signatures and implies that few, if any, of the studied inclusions can be considered primary condensates. All studied inclusions are enriched in light Ca isotopes ( $\sim -0.2$  to  $-2.8\%$ o/amu), but only two show correspondingly light Ti isotopes. Studied inclusions exhibit both heavy and light Ti isotope enrichments ( $\sim 0.3$  to  $-0.4\%$ o/amu). These refractory element isotopic signatures, therefore, suggest admixture and reprocessing of earlier formed materials with distinct condensation histories. Along with coordinated measurements of <sup>50</sup>Ti isotopic anomalies, which span a range from  $\sim 0$  to  $\sim 40$  epsilon-unit excesses, the comparison of measured and modeled fractionation of Ca and Ti isotopes provides a powerful approach to understanding primitive nebular processes and environments in the protoplanetary disk. Remarkable evidence for Ca isotopic zoning within a typical Type B1 inclusion exemplifies the potential record of the earliest solar nebula that is likely lost and/or overprinted in the isotopic compositions of more volatile elements (e.g., Mg, Si, and O) by later modification processes.

Published by Elsevier B.V. This is an open access article under the CC BY-NC-ND license (<http://creativecommons.org/licenses/by-nc-nd/4.0/>).

## 1. Introduction

Calcium-, aluminum-rich refractory inclusions (CAIs) are among the oldest surviving solids in the Solar System. Their chemical and isotopic compositions provide a record of the conditions present in the protoplanetary disk where they formed and guide our understanding of how solids formed in the solar nebula, an important step in the eventual process of planet building. Thermal events that drove evaporation and condensation in the solar nebula resulted in significant mass-dependent isotopic variations in CAIs (e.g., Clayton and Mayeda, 1977; Wasserburg et al., 1977; Niederer and Papanastassiou, 1984; Niederer et al., 1985; Davis et al., 1990; Nagahara and Ozawa, 2000; Richter et al., 2002; Shahar and Young, 2007; Yamada et al., 2006; Young et al., 1998). The magnitudes of these effects are primarily controlled by chemical volatility. While evaporation/sublimation is well explained by both theory and experimental work to produce enrichments in

the heavy isotopes that are often exhibited by the moderately refractory elements Mg and Si (e.g., Young et al., 2002), less is understood about the effects of condensation. Because the isotopic effects of condensation are likely to be complicated (e.g., Niederer and Papanastassiou, 1984 and Uyeda et al., 1991), it is unknown if any CAI is a primary condensate that retains evidence of its primordial formation history.

The approach of this study is to compare the isotopic signatures of the refractory elements Ca and Ti to each other and to moderately refractory elements more generally, and to evaluate the results in the context of a theoretical condensation model. Many existing CAI studies target the isotopic composition of an individual element, which upon comparison to the record of other elements often reveal conflicting interpretations. Along with measured <sup>50</sup>Ti anomalies, these divergent signatures may indicate real differences in their formation and/or may reflect artifacts produced by comparing the compositions of early formed solids with unrelated histories. This uncertainty can be critically addressed by our coordinated multi-isotopic approach of a common suite of CAIs, which builds on the pioneering work of Niederer and Papanastassiou (1984), Niederer et al. (1985), and Papanastassiou and Brigham (1989). Additionally, our novel theoretical approach

\* Corresponding author.

E-mail address: [Justin.I.Simon@NASA.gov](mailto:Justin.I.Simon@NASA.gov) (J.I. Simon).

<sup>1</sup> Now at Department of Earth and Environmental Sciences, Boston College, Chestnut Hill, MA, USA.

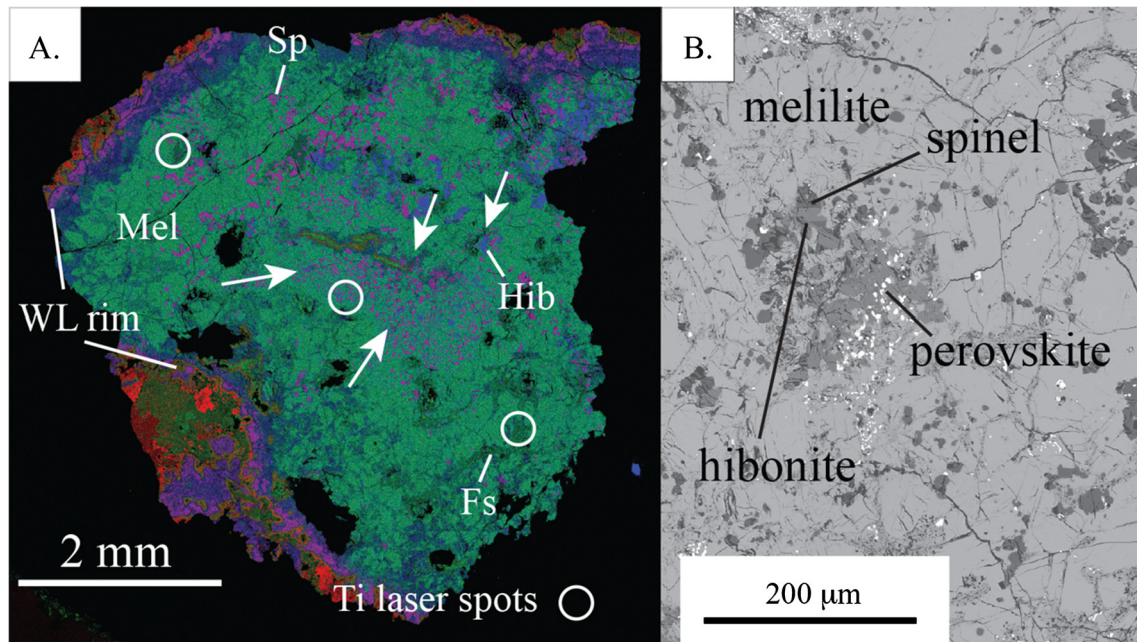


**Fig. 1.** (A) False color (RGB = Mg–Ca–Al) X-ray scanning electron microscope image of nearly intact coarse-grain Type A inclusion EK5-2-1R. Primary melilite (Mel), fassaite (Fs), Spinel (Sp) ± hibonite (Hib) are shown. Secondary sodalite and nepheline located at the outer margin of the melilite interior. Wark-Lovering (WL) rim surrounds interior. Some olivine-rich host material outside of rim seen. Arrows indicate “mélange” of accessory hibonite, perovskite, and spinel grains concentrated towards the inclusion core. (B) Back-scattered electron (BSE) image showing representative refractory mineral mélange within melilite interior.

to the condensation problem affords a self-consistent model for Ca and Ti (as well as Mg and Si) that allows a direct comparison to the measured isotopic compositions of the studied CAIs. This comparison helps us evaluate the effects of condensation and the overall formation history of these objects. In particular, using Ca and Ti to understand the isotopic effect of condensation will allow us to more accurately assess the initial isotopic ratios of the more volatile Mg and Si potentially overprinted by later evaporation events. Furthermore, these results allow us to assess whether a given CAI is a primary condensate from a homogeneous solar gas or instead represents a mixture of materials from a variety of early reservoirs. Thus, these results can be used to understand key nebular processes and environments in the protoplanetary disk that CAI compositions recorded as they formed.

## 2. Samples

A diverse group of 6 inclusions from two CV3 meteorites were studied. The suite of samples included: a Type A CAI (EK5-2-1R), a Type B1 CAI (AL4884), two fine-grained inclusions (3B3 and 461 B), and a forsterite-bearing Type B CAI SJ101 from Allende, and a “reworked” Type B CAI (Crucible) from Northwest Africa (NWA 2364). Ca isotope measurements were also performed on a range of planetary materials for reference, including an Allende chondrule, terrestrial basalts and minerals (melilite and augite), and lunar basalts (Apollo samples 12051, 15555, 70035, 70215, 74205, 75015, and 75075). The Smithsonian mineral standards were prepared from rock fragments that were gently crushed, hand-picked, and imaged by SEM, to avoid mixed mineral phases, prior to subsequently being hand powdered and dissolved. The fine-grained 3B3 and 461 B, coarse-grained Type A EK5-2-1R, and chondrule all come from slabs cut from a single sample of Allende.

In general, the studied CAIs exhibit textures and mineralogy that are typical for their sub-type classifications. Exceptions include apparent “mélanges” of accessory refractory hibonite and perovskite (±spinel) within the melilite interior of Type A CAI EK5-2-1R (Fig. 1) and the potentially reworked nature of Type B CAI Crucible (Friedrich et al., 2005). Similar to other coarse-

grained Allende CAIs, EK5-2-1R exhibits some secondary sodalite and nepheline at the outer edge of its melilite interior. In Fig. 1, EK5-2-1R appears to be about  $3 \times 3$  mm, but this sample is a non-diametric slice of a previously much larger ( $\sim 10 \times 10$  mm) inclusion (Harper et al., 1990). Crucible, 18 mm in its largest apparent diameter, is cup shaped (hence it has been called “the Crucible”) and envelops a portion of the host chondrite (Friedrich et al., 2005). Crucible contains coarsely grained melilite, fassaite, and primary anorthite, with abundant euhedral spinel heterogeneously disturbed throughout. Some anorthite has been altered to secondary melilite (Friedrich et al., 2005). AL4884 is an  $\sim 6 \times 10$  mm CAI with a heavily microfaulted surface that has been studied extensively by Bullock et al. (2013). The core of AL4884 contains the typical abundant coarse-grained melilite, fassaite, and anorthite of Type B1 inclusions. Its melilite mantle is  $\sim 250$ – $500$   $\mu\text{m}$  thick and consists mainly of gehlenitic melilite and minor spinel (Bullock et al., 2013). The microfractures across AL4884 are filled with secondary alteration and there are patchy areas of alteration within the CAI consistent with at least one previous secondary mineralization event. AL4884 was selected for this work in part because of its large size and in part because its pyroxene is particularly Ti-rich ( $\sim 5$ – $17$  wt.%  $\text{TiO}_2$ , Bullock et al., 2013). SJ101 is a very large  $\sim 15 \times 25$  mm sized, forsterite-bearing Type B CAI described in detail by Petaev and Jacobsen (2009). It consists of coarse-grained grossular, melilite, anorthite, and clinopyroxene crystals separated by sinuous finer-grained forsterite-, clinopyroxene-rich bands. Small spinel grains enclosed in the silicates are distributed homogeneously throughout the inclusion. Minimal amounts of andradite and nepheline are observed in cavities and at the edge of the inclusion. The image shown of the fine-grain inclusion 3B3 in Fig. 2 is a fragment of a large CAI that was originally at least  $\sim 10 \times 10$  mm in size. It is comprised of  $\sim 5$ – $10$   $\mu\text{m}$  sized spinel, hibonite, and alkali-rich melilite. The fine-grained CAIs lack obvious Wark-Lovering rims (Wark and Lovering, 1977). Fine-grained CAI 461 B is relatively small, only about  $\sim 250 \times 500$   $\mu\text{m}$  in size. Its hibonite ‘mantle’ is  $\sim 100$   $\mu\text{m}$  thick. It contains spinel and hibonite grains within its aggregate interior.

### 3. Methods

#### 3.1. Theoretical mass-dependent fractionation models

We considered the isotopic consequences of condensation from a nebular gas in terms of the kinetics of condensation, the degree of undercooling, and potential reservoir effects. While it is possible to directly measure fractionation factors for evaporation ( $\alpha_{\text{evap}}$ ) in the laboratory, this is not the case for condensation fractionation factors ( $\alpha_{\text{cond}}$ ). Instead, a condensation model is needed to indirectly obtain  $\alpha_{\text{cond}}$ . Invoking the law of mass action, we make use of the relationship  $\alpha_{\text{eq}} = \frac{\alpha_{\text{cond}}}{\alpha_{\text{evap}}}$ . Equilibrium fractionation factors ( $\alpha_{\text{eq}}$ ) can be calculated, allowing us to solve for  $\alpha_{\text{cond}}$ . This model considers the possibility for near-equilibrium insertion of condensing atoms and molecules where undercooling is minimal.

Kinetic fractionation during condensation depends upon the relative roles of collisional frequency (between molecular species and the grain surface), compared to the ability of a molecule to incorporate into the condensed phase structure (Simon and DePaolo, 2010). Partition of the lighter isotopes into the condensates is favored when collisional frequency is the dominant controlling effect.

Ultimately, the relative importance of equilibrium versus the potentially much larger kinetic effects in the isotope fractionation depends on the degree of “overstepping” thermodynamic equilibrium as measured by the saturation index  $S_i = P_i/P_{i,\text{eq}}$  with  $S_i > 1$  implying condensation.  $S_i$  can be equated with a temperature difference (i.e., undercooling) from the equilibrium condensation temperature using the Van’t Hoff equation and the enthalpy for the condensation reaction (Simon and DePaolo, 2010). Combining these we arrive at a model for fractionation during condensation:

$$\alpha_{\text{cond}} = \frac{\alpha_{\text{eq}}\alpha_{\text{kin}}S_i}{\alpha_{\text{eq}}(S_i - 1) + \alpha_{\text{kin}}} \quad (1)$$

where

$$\alpha_{\text{kin}} = \alpha_{\text{evap}}\alpha_{\text{eq}}\sqrt{\frac{m_i}{m'_i}} \quad (2)$$

with  $m_i$  being the mass of the lighter isotopic species of interest and  $m'_i$  being the mass of the heavier isotopic species.

#### 3.2. Analytical approaches

##### 3.2.1. Ca isotope analysis by thermal ionization mass spectrometry

Mass dependent Ca isotopic compositions are measured by a  $^{42}\text{Ca}$ – $^{48}\text{Ca}$  double spike method on a Thermo Fisher Scientific Triton thermal ionization multi-collector mass spectrometer (TIMS) housed in the Center for Isotope Cosmochemistry and Geochronology at NASA Johnson Space Center (Fig. 3). The specific procedures including sample loading and analysis methodologies are similar, but improved on those described by Simon and DePaolo (2010). Using a parafilm “dam” about 3  $\mu\text{g}$  of purified calcium is loaded in nitrate form with  $\text{H}_3\text{PO}_4$  on an outgassed Re filament. The calcium is ionized in a typical double filament configuration. A multi-step cup configuration sequence is used in order to obtain  $^{40}\text{Ca}$ ,  $^{42}\text{Ca}$ ,  $^{43}\text{Ca}$ ,  $^{44}\text{Ca}$ , and  $^{48}\text{Ca}$  ion beams using Faraday collectors with  $10^{11} \Omega$  resistors and to obtain potential mass interferences using electron multipliers. The magnitudes of potential interferences from  $^{40}\text{K}$  and  $^{48}\text{Ti}$  (determined by measuring  $^{39}\text{K}$  and  $^{49}\text{Ti}$ , respectively) are found to be insignificant; no corrections were applied. Each analysis consists of 200 cycle measurements. Instrumental mass discrimination corrections based on the difference between the sample subtracted  $^{42}\text{Ca}/^{48}\text{Ca}$  ratio and the double tracer composition are calculated offline for each cycle to account for possible changes in the mass discrimination in the spectrometer over

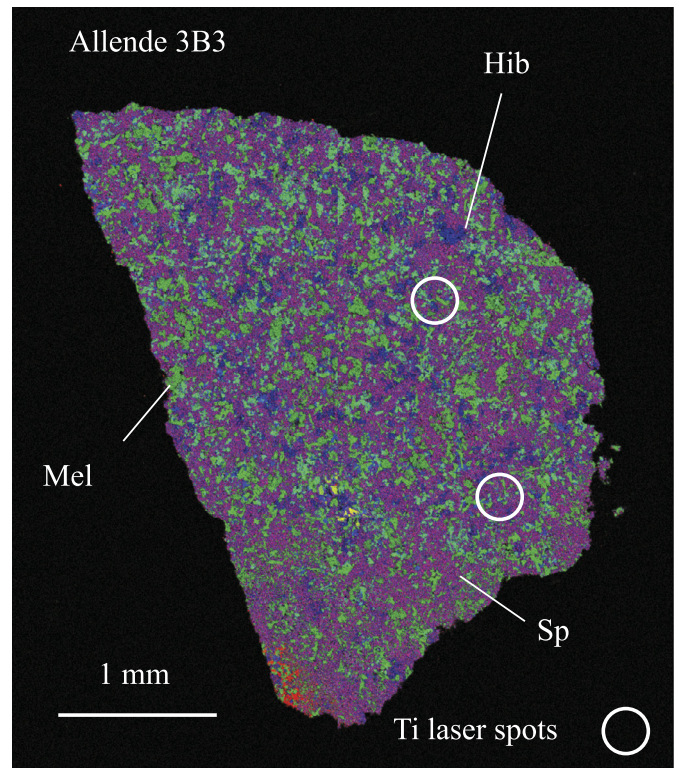


**Fig. 2.** False color (RGB = Mg–Ca–Al) X-ray scanning electron microscope image of fragment of fine-grain alkali-rich Allende inclusion 3B3. Spinel (Sp, purple), hibonite (Hib, blue), melilite (Mel, green) dominate mineral assemblage. Red material at bottom indicative of olivine-rich host material. The image is of a fragment of a large inclusion ( $\sim 10 \times 10$  mm). (For interpretation of the references to color in this figure, the reader is referred to the web version of this article.)

the duration of each  $\sim 3$  hour analysis. An exponential law is used for the instrumental mass discrimination corrections. Given that the magnitude of Ca isotopic anomalies in common Types A and B inclusions are small (Niederer and Papanastassiou, 1984; Simon et al., 2009; Shiller et al., 2015) we assume that their Ca compositions are normal, except for the mass fractionation effects. This study follows the approach of Simon and DePaolo (2010) who report sample measurements relative to the normal value of most planetary materials (igneous materials from Earth, Moon, Mars, and differentiated achondrites). After accounting for the spike and mass discrimination, the “absolute”  $^{40}\text{Ca}/^{44}\text{Ca}$  in the sample is normalized so that  $^{42}\text{Ca}/^{44}\text{Ca} = 0.31221$  (Russell et al., 1978) and expressed in delta notation where:

$$\delta^{44}\text{Ca}/^{40}\text{Ca} = \left[ \frac{(^{44}\text{Ca}/^{40}\text{Ca})_{\text{sample}}}{(^{44}\text{Ca}/^{40}\text{Ca})_{\text{normal}}} - 1 \right] \times 1000. \quad (3)$$

In this notation, positive values indicate enrichments in the heavier Ca isotopes and negative values indicate enrichments in the lighter isotopes. Measured seawater, BCR-1 & 2, and SRM915a & b standards, as well as, melilite and augite terrestrial minerals (from the Smithsonian Institute) yielded their expected values (Table 1). All samples were replicated and yielded internal precisions similar to the  $\sim 0.04$  to  $0.06\%$  2 standard errors (SE) of the rock standards. The weighted averages of replicate measurements and their 2 SE are included in Table 1.

##### 3.2.2. Ti isotope analysis by laser ablation multiple-collector inductively coupled plasma-source mass spectrometry

Titanium isotope analyses were conducted using the LA-MC-ICPMS (Thermo Fisher Scientific Neptune<sup>TM</sup>) housed at UCLA. Most

**Table 1**  
Summary of Ca and Ti isotope data.

Sample	Description	Sample wt. (mg) <sup>f</sup>	$\delta^{44}\text{Ca}/^{40}\text{Ca}$ (seawater scale)	$\delta^{44}\text{Ca}/^{40}\text{Ca}$ (chondritic scale)	$\delta^{44}\text{Ca}/^{40}\text{Ca}$ (SRM915a scale)	2 SD	2 SE <sup>d</sup>	$\delta^{49}\text{Ti}/^{47}\text{Ti}$ (laser)	2 SE	$\varepsilon(^{50}\text{Ti}/^{47}\text{Ti})$ (laser)	2 SE	Spots (laser)	$\varepsilon(^{50}\text{Ti}/^{47}\text{Ti})$ (TIMS <sup>c</sup> )	2 SE
461 3B3	fine-grained Type A	1.19	−12.11	−11.31	−10.34		0.03	0.64	0.11	6.2	1.7	$n = 10$	13.2	1.2
EK5-2-1R	coarse-grained Type A fassiatae hibonite/per- ovskite/spinel	28.34	−1.89	−1.09	−0.12		0.12	−0.10 −0.43 0.23	0.37 0.28 0.42	1.0 1.5 0.4	0.8 0.5 1.1	$n = 6$ $n = 3$ $n = 3$	0.0	1.0
461, 13, 2 slab B	fine-grained Type A, hibonite-rich mantle	0.23	−1.61	−0.81	0.16		0.03	−0.73	0.42	41.6	5.2	$n = 7$		
NWA 2364 “Crucible”	avg. reworked coarse-grained Type B core	1.15	−1.41	−0.61	0.36	0.16	0.08	0.15	0.13	6.5	2.4	$n = 1$		
AL4884	margin	0.56	−1.37	−0.57	0.40		0.02							
	coarse-grained Type B1, core	0.41	−1.46	−0.66	0.31		0.14							
	coarse-grained Type B1, outer core	0.58	−2.46	−1.66	−0.69		0.08	0.15	0.13	8.8	1.7	$n = 6$		
SJ101 <sup>a</sup>	coarse-grained Type B1, mel mantle	0.19	−2.30	−1.50	−0.53		0.03							
	coarse-grained Type B1, mel mantle	0.27	−1.77	−0.97	0.00		0.07							
	Fo-bearing	?	−3.50	−2.70	−1.73		0.05	0.05	0.11	11.0	1.5	$n = 5$		
Other data														
461, 13, 2slab_D	complex chondrule	0.40	−0.80	0.00	0.97		0.06							
BCR-2	basalt		−0.90	−0.10	0.87	0.08	0.06							
BCR-1 <sup>b</sup>	basalt		−0.89	−0.09	0.88	0.05	0.03							
Allende	carbonaceous chondrite, bulk		−1.22	−0.42	0.55		0.11							
103140 (terrestrial)	akermanite mineral separate		−0.86	−0.06	0.91		0.15							
164905 (terrestrial)	augite mineral separate		−0.83	−0.03	0.94		0.06							
lunar (7 samples)	basalt, high and low Ti		−0.78	0.02	0.99	0.14	0.03							
SRM915a ( $n = 9^e$ )	carbonate		−1.76	−0.96	0.01	0.13	0.04							
SRM915b ( $n = 10$ )	carbonate		−0.96	−0.16	0.81	0.18	0.06							
Seawater ( $n = 3$ )	IAPSO standard		−0.01	0.79	1.76		0.16							
USNM 83191	rutile							−0.12	0.33	−2.1	3.4	$n = 3$		
P10	synthetic glass							−0.30	0.14	1.4	1.4	$n = 6$		

<sup>a</sup> Ca isotope data for CAI SJ101 from Huang et al. (2012), Harvard.

<sup>b</sup> Ca isotope data for BCR-1 from Simon and DePaolo (2010), UC Berkeley.

<sup>c</sup> Ti isotope data for 3B3 and EK5-2-1 from Harper et al. (1990), NASA JSC.

<sup>d</sup> All unknowns and terrestrial materials replicated.

<sup>e</sup> SRM915a internal standard ran in 2015, 3 analyses during instrument use for this study.

<sup>f</sup> Sample weights for 42–48 Ca isotope TIMS analyses; rock and mineral standard and reference materials were approximately 25 mg.

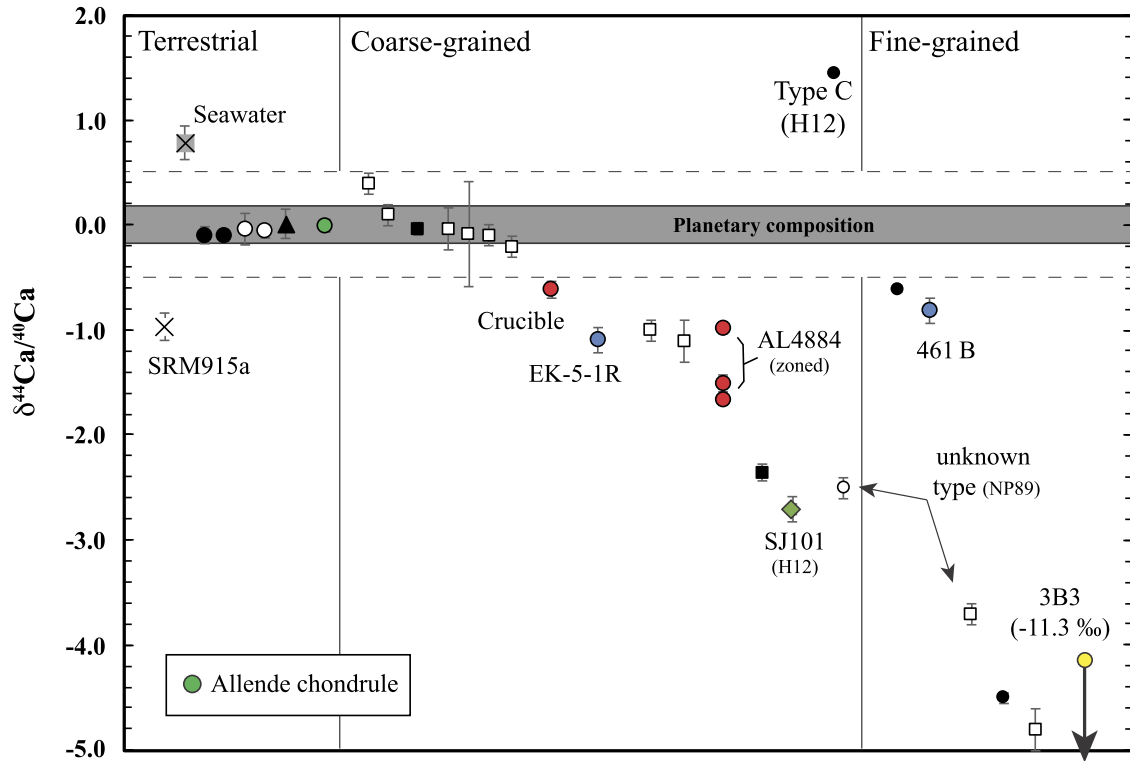


**Fig. 3.** Plot shows double spike TIMS measurements of mass dependent calcium isotope compositions of CAIs and other planetary materials. Reported uncertainties are 2 SE and often less than the symbol size. Standard reference materials show 2 SD external reproducibility. Open symbol CAI data come from [Niederer and Papanastassiou \(1984\)](#) (NP84). Black CAI and SJ101 (green diamond) data come from [Huang et al. \(2012\)](#) (H12). Measured terrestrial minerals, lunar basalts, and chondrule (this study) lie within the range of planetary materials reported by [Simon and DePaolo \(2010\)](#). For reference, FUN inclusions range from  $-27$  to  $+15$ ‰ and the range ( $\pm 0.5$ ‰) delineated by the horizontal dashed lines reflects the stated confidence interval of individual measurements in NP84. (For interpretation of the references to color in this figure, the reader is referred to the web version of this article.)

analyses in the CAIs are dominated by the Ti-bearing pyroxene phase. Some measurements also include perovskite and minor hibonite as well. All mass-dependent  $^{49}\text{Ti}/^{47}\text{Ti}$  isotope ratios measured in this study are reported in per mil deviations ( $\delta^{49}\text{Ti}/^{47}\text{Ti}$ ) from a terrestrial rutile reference material (USNM 83191).

$$\delta^{49}\text{Ti}/^{47}\text{Ti} = \left[ \frac{(^{49}\text{Ti}/^{47}\text{Ti})_{\text{sample}}}{(^{49}\text{Ti}/^{47}\text{Ti})_{\text{normal}}} - 1 \right] \times 1000. \quad (4)$$

It is generally agreed that in common Types A and B inclusions  $^{49}\text{Ti}/^{47}\text{Ti}$  is effectively free from nuclear anomalies at the 0.1‰ level or greater ([Zhang et al., 2011](#)) and we have demonstrated that we can measure  $^{49}\text{Ti}/^{47}\text{Ti}$  ([Fig. 4](#)) free from matrix effects within our analytical precision of  $\sim 0.3$ ‰ (2 SE). Ru and Mo doubly-charged interferences are well below detection and have no influence. The lack of matrix effects is illustrated here by comparing our UCLA Glass #5 (P10) standard (fassaite composition, previously measured for Ti isotopes by [Chen et al., 2009](#)) with pure  $\text{TiO}_2$  ([Fig. 4](#)); there is limited fractionation among terrestrial materials in general ( $< 0.1$ ‰, e.g., [Zhang et al., 2011](#); [Zhu et al., 2002](#)) and we see no spurious fractionation between this fassaite glass and pure  $\text{TiO}_2$ .

There is a rich history of measurements of  $^{50}\text{Ti}$  isotope effects in CAIs, including some recently reported results using laser ablation ([Niederer et al., 1980, 1981, 1985](#); [Papanastassiou and Brigham, 1989](#); [Niemeyer, 1988](#); [Chen et al., 2009](#); [Leya et al., 2009](#); [Trinquier et al., 2009](#); [Zhang et al., 2012](#); [Williams et al., 2016](#)). These studies find that mass-fractionation-corrected  $^{50}\text{Ti}$  anomalies, expressed as  $\epsilon^{50}\text{Ti}$  (parts per 10,000) in common Types A and B inclusions are generally between  $+2$  and  $+15$  with the most typical values near  $+10$ . Although laser ablation sampling of  $^{50}\text{Ti}$  excesses has been reported ([Williams et al., 2012](#)) there are still no systematic *in situ* studies of potential correlations between

mass-fractionation effects and the large  $\epsilon^{50}\text{Ti}$  in CAIs. In order to measure  $^{50}\text{Ti}/^{47}\text{Ti}$  excesses we peak strip interferences from  $^{50}\text{Cr}$  and  $^{50}\text{V}$  by monitoring  $^{52}\text{Cr}$  and  $^{51}\text{V}$  during each analysis and correcting for instrumental fractionation in the usual way ( $\beta$  exponents characterizing instrumental fractionation). The validity of this stripping approach can be seen by the accuracy and reproducibility of a range of standard materials, [Fig. 5](#).

Ion currents for  $^{47}\text{Ti}^+$ ,  $^{49}\text{Ti}^+$ ,  $^{50}\text{Ti}^+$ ,  $^{51}\text{V}^+$ , and  $^{52}\text{Cr}^+$  were measured for each laser run on Faraday collectors with  $10^{11} \Omega$  resistors. Each measurement comprises 10 cycles of 4s integrations. The mass resolving power ( $m/\Delta m$ ) was 7000 or greater for these analyses. The effects of instrumental fractionation were corrected for by sample-standard bracketing. An instrumental mass fractionation factor,  $\alpha_{\text{inst}}$ , was also calculated by comparing measured  $^{49}\text{Ti}/^{47}\text{Ti}$  to a nominal ratio of 0.74500. This instrumental fractionation factor was used to derive an exponent  $\beta$  for the general fractionation law ( $\alpha_{\text{inst}} = (m_2/m_1)^\beta$ ) that was then used for both V and Cr with the relationship  $\beta = \ln(\alpha_{\text{inst}})/\ln(m_{49}/m_{47})$  where  $m_i$  refers to the atomic mass of interest. Typical values for  $\alpha_{\text{inst}}$  and  $\beta$  for the operating conditions used in this study are 1.083 and 1.91, respectively. We find that these values pertain for Fe as well as for Ti and are characteristic of instrumental conditions at UCLA for transition metals in this mass range. The Ti-derived fractionation law was applied to the measured  $^{51}\text{V}^+$  and  $^{52}\text{Cr}^+$  to derive  $^{50}\text{V}^+$  and  $^{50}\text{Cr}^+$  ion currents interfering with that for  $^{50}\text{Ti}^+$ . These interferences were subtracted from the mass/charge = 50 ion current to obtain the  $^{50}\text{Ti}^+$  ion current.

An excimer laser with 193 nm wavelength and  $\sim 4$  ns pulse length (Photon-Machines, Analyte.193) was operated at fluences of  $\sim 28 \text{ J/cm}^2$  for ablation. For this study the laser was operated at pulse repetition rates of between 1 and 6 Hz using spot sizes of 28 to 172  $\mu\text{m}$  (typical ablation pit depths are  $\sim 25$  to 30  $\mu\text{m}$ ), with the

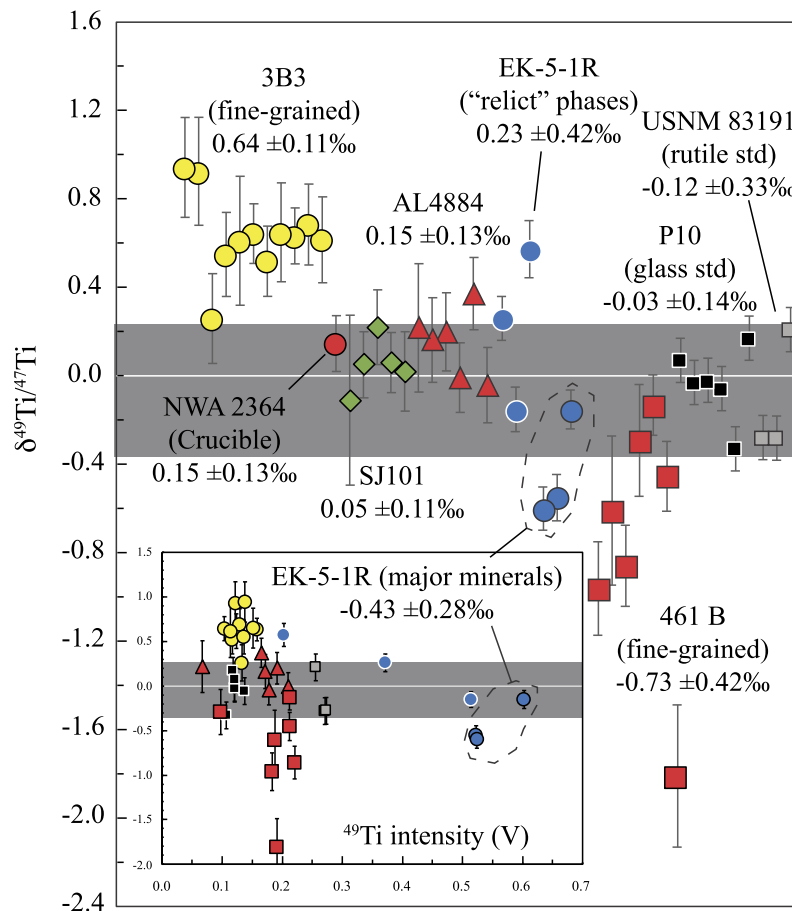


**Fig. 4.** Plot of laser ablation MC-ICPMS spot analyses of mass dependent titanium isotope compositions for studied refractory inclusions. Symbols as in Fig. 3. IntraCAI heterogeneity in fine-grained CAIs (3B3 and 461 B) and in EK-5-1R (relict phases are heavy and major minerals light) exist. Inset shows that isotope effects are independent of measured  $^{49}\text{Ti}$  intensity. Uncertainty of individual measurements are 2 SE internal precision. Standard materials shown for comparison.

combination of pulse rate and spot size depending on the concentration of Ti. Tests of the effects of pulse rate and spot size showed no correlations with measured isotope ratios. The laser ablation sample chamber is flushed with He (0.29 L/min) and mixed with Ar (0.69 L/min) and  $\text{N}_2$  (8 ml/min) in a mixing cell just prior to introduction into the plasma.

#### 4. Analytical results

All studied CAIs have  $\delta^{44}\text{Ca}/^{40}\text{Ca}$  values less than “normal” planetary-like compositions ( $\sim 0\text{‰}$ ), similar to the isotopically “light” values reported in the early studies of Russell et al. (1978) and Niederer and Papanastassiou (1984) and more recently by Huang et al. (2012). These signatures are also consistent with the enriched light isotopic compositions in Eu, Sr, and Ba reported by Moynier et al. (2006, 2010, 2015). None of the objects studied in this work yield positive  $\delta^{44}\text{Ca}/^{40}\text{Ca}$  values (cf. Niederer and Papanastassiou, 1984; the Type C inclusion of Huang et al., 2012). Measured CAI  $\delta^{44}\text{Ca}/^{40}\text{Ca}$  values range from approximately  $-0.6$  to  $-11.3\text{‰}$  (a majority yielded values between  $-0.6$  to  $-1.7\text{‰}$ ) that are clearly resolved from measured planetary silicate materials including the Allende chondrule ( $0.00 \pm 0.06\text{‰}$ , 2 SE), terrestrial basalts ( $-0.10 \pm 0.06\text{‰}$ , 2 SE), terrestrial melilite ( $-0.06 \pm 0.15\text{‰}$ , 2 SE), terrestrial augite ( $-0.03 \pm 0.06\text{‰}$ , 2 SE), and lunar basalts ( $0.02 \pm 0.03\text{‰}$ , 2 SE). The value measured for the second carbonate standard SRM915b was slightly less than planetary ( $-0.16 \pm 0.06\text{‰}$ , 2 SE) and IAPSO seawater standard was higher ( $0.79 \pm 0.16\text{‰}$ , 2 SE) as is expected. The CAIs exhibit values lower than the value measured herein for bulk Allende powder

( $-0.42 \pm 0.11\text{‰}$ , 2 SE) reported previously by Simon and DePaolo (2010); Valdes et al. (2014) (Fig. 3, Table 1).

Due to their relatively large size, subsamples of Type B inclusions Crucible and AL4884 were obtained by micromilling. No resolvable difference was observed between the core and outer edge of Crucible,  $\delta^{44}\text{Ca}/^{40}\text{Ca} = -0.57 \pm 0.02\text{‰}$  (2 SE) and  $-0.66 \pm 0.14\text{‰}$  (2 SE), respectively. However, a clear difference can be seen across AL4884, with the core yielding  $\delta^{44}\text{Ca}/^{40}\text{Ca} = -1.66 \pm 0.08\text{‰}$  (2 SE), outer core yielding  $-1.50 \pm 0.03\text{‰}$  (2 SE), and the melilite mantle yielding  $\delta^{44}\text{Ca}/^{40}\text{Ca} = -0.97 \pm 0.07\text{‰}$  (2 SE; Fig. 6). To our knowledge no evidence of intraCAI mass dependent Ca isotopic heterogeneity has been reported previously in any nebular material.

In contrast to the “light”  $\delta^{44}\text{Ca}/^{40}\text{Ca}$  values measured, most measured  $\delta^{49}\text{Ti}/^{47}\text{Ti}$  ratios in the studied CAIs have “normal” compositions, although small mass dependent Ti isotope effects exist. The Ti isotopic compositions of Crucible, AL4884, and SJ101 (i.e.,  $\delta^{49}\text{Ti}/^{47}\text{Ti} = 0.06$  to  $0.15\text{‰}$ ), are unresolvable from a planetary value, see Fig. 4. A similar value was measured for the accessory hibonite/perovskite/spinel mélange in EK5-2-1R ( $0.23 \pm 0.32\text{‰}$ , 2 SE). The primary phases within the interiors of EK5-2-1R and 461 B appear to exhibit slightly lower  $\delta^{49}\text{Ti}/^{47}\text{Ti}$  values of about  $-0.40$  and  $-0.70\text{‰}$ , respectively. The fine-grained CAI 3B3 has a slightly positive  $\delta^{49}\text{Ti}/^{47}\text{Ti}$  value ( $0.64 \pm 0.10\text{‰}$ , 2 SE) that is resolvable from the normal planetary composition. It should be noted that measurements of Ti isotope mass fractionation in CAIs date back to the early 1980’s. Niederer et al. (1985) found CAIs to be between  $+0.2$  to  $+1.0\text{‰}$  per amu among both normal and FUN CAIs. However, reports at conferences of wider ranges in  $^{49}\text{Ti}/^{47}\text{Ti}$  of  $-2.7$  to  $+4.0$  exist (Zhang et al., 2012).

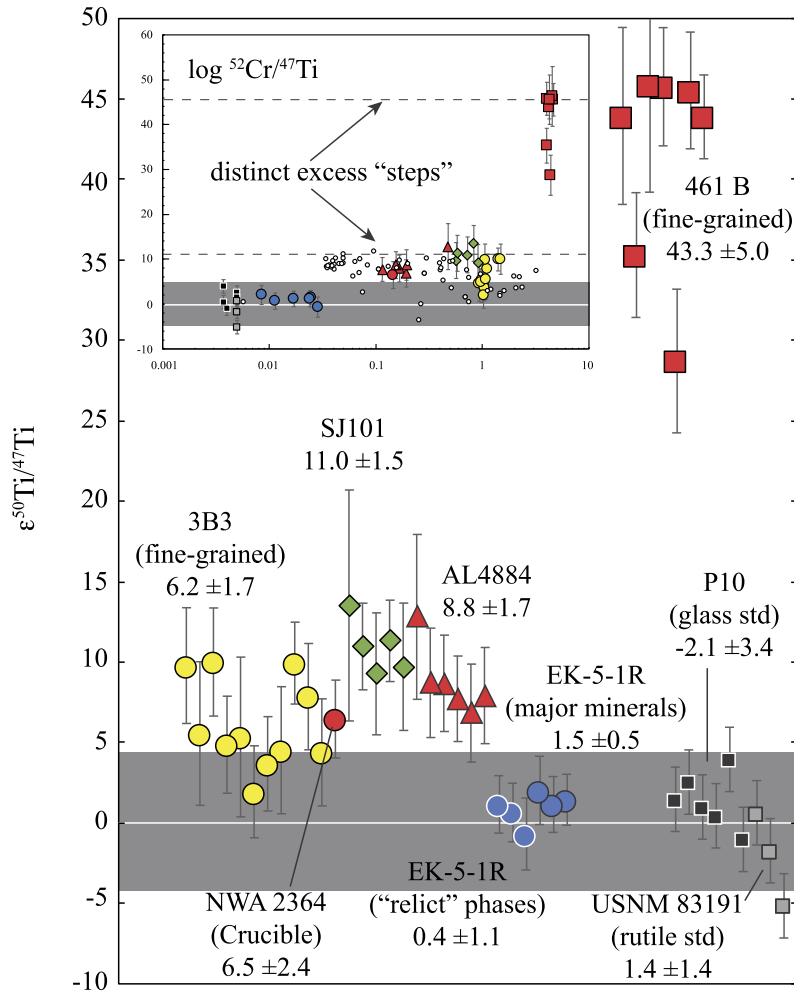


**Fig. 5.** Plot of laser ablation MC-ICPMS spot analyses of  $\epsilon^{50}\text{Ti}/^{47}\text{Ti}$  titanium isotopic anomalies in studied refractory inclusions. Symbols as in Fig. 3. Inset shows that measured  $^{50}\text{Ti}$  isotope anomalies define clear plateaus that are not easily related to Cr abundance (i.e., Cr/Ti ratio). Data report by Jordan et al. (2017) shown as small circles. Uncertainty of individual measurements are 2 SE internal precision. Standard materials shown for comparison.

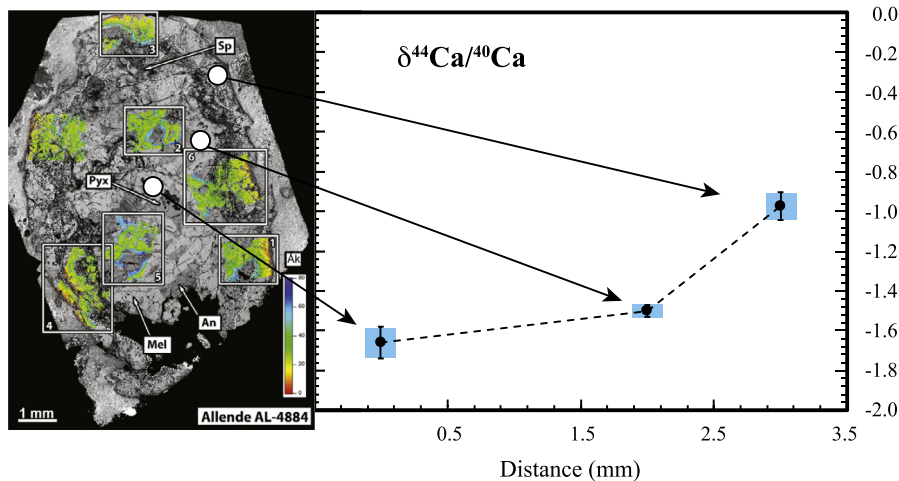


**Fig. 6.** Calcium isotopic zoning across Type B CAI AL-4884. Analytical measurements across the entire inclusion exhibit negative  $\delta^{44}\text{Ca}/^{40}\text{Ca}$  values, but these values get higher, i.e., heavier towards the edge of the inclusion. Data are shown relative to the planetary composition (e.g., bulk silicate Earth  $\sim 0\%$ ). Image at left shows micromilling subsample locations and compositional zoning in melilite from Bullock et al. (2013).

Anomalous  $^{50}\text{Ti}/^{47}\text{Ti}$  isotope effects ( $\epsilon^{50}\text{Ti}$ ) were also measured by laser ablation MC-ICPMS (UCLA). Most measured  $^{50}\text{Ti}$  excesses were found to be  $\sim 6$  to 13 epsilon units in the studied CAIs (Fig. 5). The measured  $\epsilon^{50}\text{Ti} = 11.3 \pm 3.0$  (2 SE) for SJ101 and the unpublished TIMS analysis measured at NASA JSC, i.e., Harper

et al. (1990) of the fine-grained CAI 3B3 of  $\epsilon^{50}\text{Ti} = 13.2 \pm 1.2$  (2 SE) represent typical values of the studied samples. These analyses are similar to those previously reported (see Fig. 7). The first exception is EK5-2-1R that appears to show little to no  $\epsilon^{50}\text{Ti}$  effect ( $1.0 \pm 0.8$ , 2 SE), which is consistent with the  $\epsilon^{50}\text{Ti}$  value of

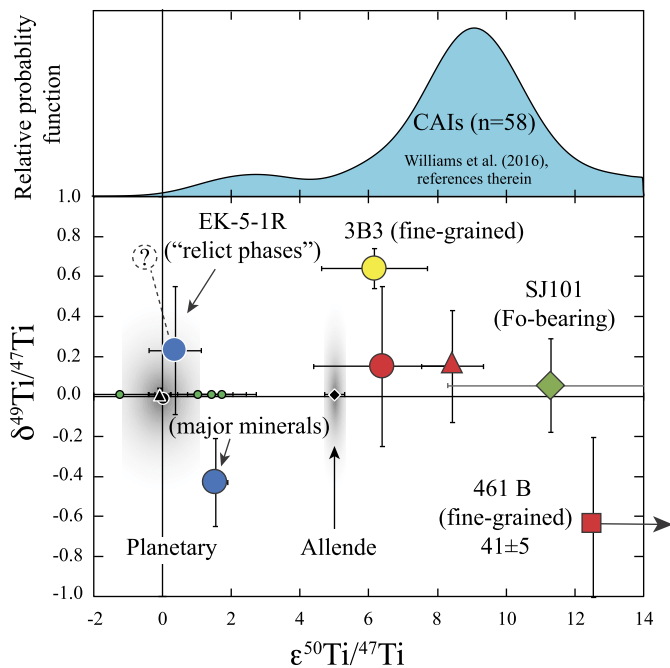


**Fig. 7.** Plot of laser ablation MC-ICPMS measurements of mass fractionated titanium  $\delta^{49}\text{Ti}/^{47}\text{Ti}$  compositions and  $\varepsilon^{50}\text{Ti}/^{47}\text{Ti}$  titanium isotopic anomalies in the studied refractory inclusions. Uncertainty are 2 SE. Symbols for CAIs as in Fig. 3. Allende whole rock = black diamond, lunar basalt = black triangle, terrestrial basalt = black circle, Allende chondrules = green circles shown. Mass dependent isotope compositions of lunar and terrestrial rocks determined by double spike solution MC-ICPMS analysis (Millet et al., 2016).  $\varepsilon^{50}\text{Ti}/^{47}\text{Ti}$  values for rocks and bulk Allende measured by MC-ICPMS (Trinquier et al., 2007, 2009, and references therein). The distribution of  $\varepsilon^{50}\text{Ti}/^{47}\text{Ti}$  values for common Types A and B inclusions (top) reported by Niederer et al. (1980, 1981, 1985), Trinquier et al. (2009), Leya et al. (2009), Chen et al. (2009), Williams et al. (2016), and this study is shown. (For interpretation of the references to color in this figure, the reader is referred to the web version of this article.)

$0.0 \pm 1.0$  (2 SE) measured by TIMS. It is noteworthy that an average of just the spots dominated by major minerals appears to exhibit a resolvable excess ( $1.5 \pm 0.5$ , 2 SE), as they also appear isotopically “light” (see above). The second exception is 461 B that exhibits a large  $\varepsilon^{50}\text{Ti}$  excess ( $41.6 \pm 5.2$ , 2 SE), which also exhibits a negative  $\delta^{49}\text{Ti}/^{47}\text{Ti}$  value (Fig. 7). This isotopic anomaly is the largest excess observed for common Types A and B CAIs, as opposed to spinel-hibonite inclusions (SHIBs), platy hibonite crystals (PLACs), and those that exhibit Fractionated and Unidentified Nuclear (FUN) isotopic properties (Wasserburg et al., 1977). Although extensive tests were made to demonstrate the validity of our peak-stripping and mass bias correction method, other investigations that employed a calibration curve to correct for interferences (Williams et al., 2016) have found that a high Ca/Ti ratio like that measured in 461 B (Fig. 5, inset) can artificially enhance the  $^{50}\text{Ti}/^{47}\text{Ti}$  ratio of up to  $\sim 10$  epsilon units. Unlike Williams et al. (2016), the peak stripping method appears to work for us because we find that the mass bias characteristic of instrumental conditions at UCLA for transition metals in this mass range are similar (see section 3.2.2). The effect in question is also much larger than 10 epsilon units and does not follow the expected linear relationship that an interference would produce.

## 5. Discussion

### 5.1. Condensation model for isotope fractionation

In order to calculate the isotope fractionation factors ( $\alpha_{\text{cond}} = R_{\text{cond}}/R_{\text{vapor}}$ ) needed to construct theoretical condensation model curves that can account for non-equilibrium conditions, one must

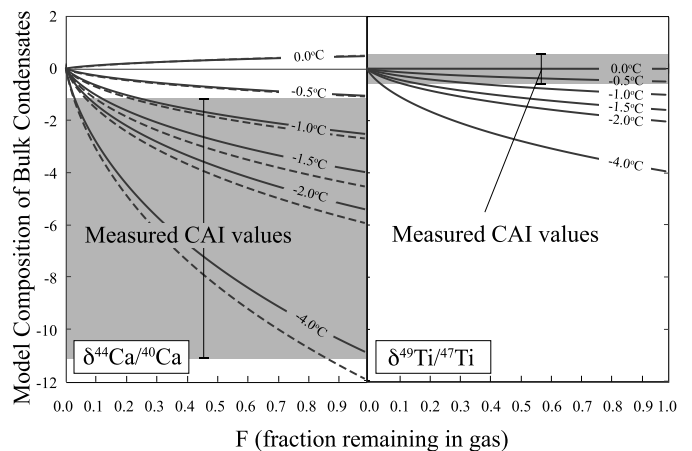


**Fig. 8.** Modeled isotopic evolution of bulk condensate compositions during Rayleigh distillation of nebular gas at 1600 K. Dashed Ca model curves represent condensation at 1525 K (see text). Ca and Ti isotopic signatures are typically depleted in heavy isotopes during non-equilibrium condensation (undercooling). Small Ca isotopic enrichments can be achieved by equilibrium condensation (left).

consider multiple processes contributing to the fractionation. As outlined in Section 3.1,  $\alpha_{\text{cond}}$  is a function of equilibrium fractionation factors ( $\alpha_{\text{eq}}$ ), fractionation associated with evaporation ( $\alpha_{\text{evap}}$ ) through the law of mass action, and fractionation related to gas phase transport ( $\alpha_{\text{trans}} = \sqrt{m/m'}$ ). Equilibrium fractionation factors ( $\alpha_{\text{eq}}$ ) can be determined by thermodynamic considerations (e.g., Simon and DePaolo, 2010). Values for  $\alpha_{\text{eq}}$  between solid and vapor can be estimated from reduced partition function ratios ( $\beta$ ), following the approach of Schauble (2011). The magnitude of fractionation is controlled mainly by the transformation from vapor to solid with the exact identity of the solid phase(s) being of less importance. For calcium models, we assume an  $\alpha_{\text{eq}}$  for the simple reaction where Ca vapor condenses to silicate (i.e., diopside). At 1600 K, the Ca  $\alpha_{\text{eq}}$  equates to 1.000477. This is justified because at realistic nebular temperatures and pressures Ca  $\gg$  CaO (Zhang et al., 2014). For titanium models, we assume equilibrium between TiO and TiO<sub>2</sub> in the vapor phase and rutile. This leads to a Ti  $\alpha_{\text{eq}}$  at 1600 K that is less than unity (0.999995). The relative abundances of the titanium gas species (TiO  $\sim 0.8$  and TiO<sub>2</sub>  $\sim 0.2$ ) are based on the equilibrium condensation calculations of the type described in Ebel and Grossman (2000). The  $\alpha$  values empirically determined for evaporation ( $\alpha_{\text{evap}}$ ) for Ca ( $\sim 0.9562$ ) and Ti ( $\sim 0.9880$ ) come from Zhang et al. (2014). The  $\alpha$  values associated with vapor transport ( $\alpha_{\text{trans}}$ ) assume collision frequency ratios for the vapor phase species involving the atomic masses in the case of calcium vapor (i.e., Ca  $\alpha_{\text{trans}} = 0.953499$ ) and the oxides TiO and TiO<sub>2</sub> for titanium vapor (i.e., Ti  $\alpha_{\text{trans}} = 0.985246$ ).

### 5.2. Isotopic reservoir effects related to distillation of nebular gas

Calculations combining equations (1)–(3) afford  $\alpha_{\text{cond}}$  values that can be used to model the magnitude of Ca and Ti isotopic fractionation effects produced by condensation of nebular gas. Although these likely oversimplify the condensation process(es) that occurred in the early Solar System, they are illustrative. Using  $\alpha_{\text{cond}}$  (e.g., from section 5.1), the magnitude of isotope fractionation that occurs as the result of the Rayleigh distillation process expected during condensation leads to the model curves shown in Figs. 8, 9 and 11. For the sake of completion both bulk and instantaneous (in section 5.3) condensation models are considered. Substitution of  $\alpha_{\text{cond}}$  into the typical bulk Rayleigh equation:

$$\delta = (\delta_0 + 1000) \left( \frac{(1 - F)^{\alpha_{\text{cond}}}}{(1 - F)} \right), \quad (5)$$

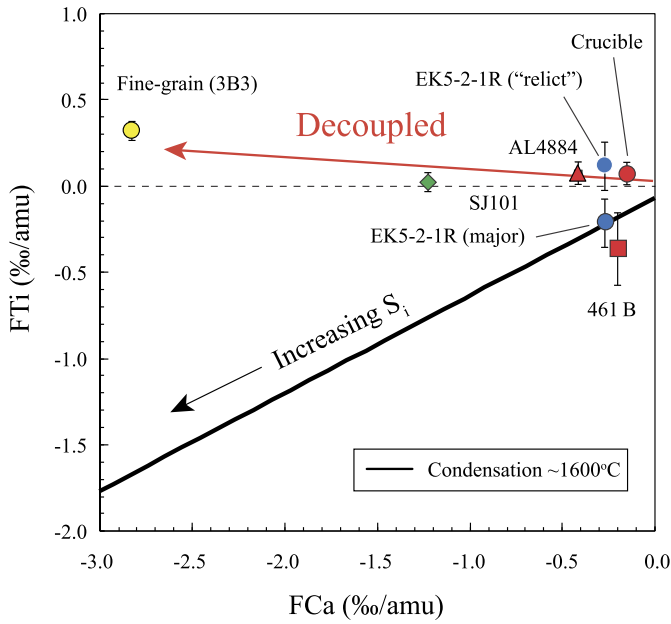


**Fig. 9.** Ca and Ti isotope data for studied inclusions plotted with mass fractionation condensation modeling shown as a function of oversaturation ( $S_i$ ) (thick solid line). All data and model results converted to a common scale for direct comparison. A general trend among Type B CAIs AL4884 (core), Crucible, SJ101, and fine-grained 3B3 (red line), can be seen but lies off the theoretical curve. CAIs EK5-2-1R (major minerals) and 461 B are consistent with theoretical fractionation.

where  $F$  is the fraction of gas remaining shows the effects of condensation where early formed nebular materials are expected to record an increased degree of light isotopic enrichment due to the depletion of the heavy isotopes by prior vapor-gas fractionation (Fig. 8). The computed relatively light Ca isotopic signatures are consistent with those measured in CAIs by Niederer and Papanastassiou (1984), Huang et al. (2012), and this study.

During equilibrium condensation (i.e., ~no undercooling), however, the Ca fractionation model calculations show that small positive mass dependent isotope effects of up to ~0.5‰ can be produced. Under equilibrium conditions there is a slight depletion of light isotopes induced by vapor-gas fractionation leading to a heavy isotope enriched gas reservoir (Fig. 8, left panel). In the case of Ca this is an especially robust result as Ca bonded to other atoms will always favor the heavy isotopes relative to the atomic Ca (i.e., logarithms of the reduced partition functions are greater than zero). In the case of the Ti isotope fractionation models there is effectively no  $\alpha_{eq}$  contribution ( $\alpha_{eq} = 0.999995$ ) because Ti is bonded to oxygen in the dominant gas species, limiting differences in reduced partition function ratios. As a result, there are no heavy isotope enrichments in the condensates at equilibrium as there are for Ca (Fig. 8, left panel). Comparison of the Ca and Ti condensation models in Fig. 8 show that the magnitudes, and in some cases the signs, of isotopic fractionations between chemically similar elements can be non-intuitive.

### 5.3. Comparison of measurements to condensation models

A comparison of the coeval Ca and Ti isotope ratios to the condensation models is shown in Fig. 9. The model curve for condensation in Fig. 9 is based on an assumption that the degree of saturation for Ca and Ti should be similar given their broadly similar condensation temperatures (Fig. 10) (i.e.,  $S_{Ca} = S_{Ti}$ ). The measured Ca and Ti isotopic fractionation effects in most of the CAIs of this study do not follow the  $S_{Ca} = S_{Ti}$  curve, suggesting a decoupling of the Ca and Ti systems in terms of saturation. Type B inclusions AL4884, Crucible, and forsterite-bearing SJ101

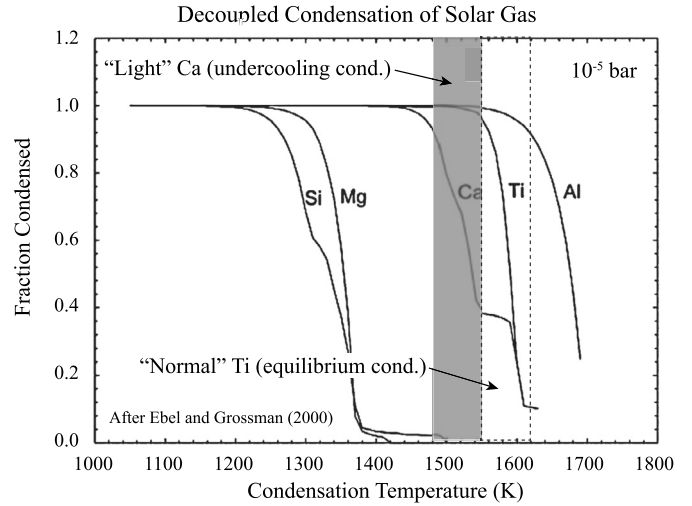


**Fig. 10.** Predicted enrichments of major rock forming elements as a function of condensation temperature (thermodynamic condensation model curves from D. Ebel). Possible decoupled history of Ca and Ti condensation of Solar gas shown that can explain the normal Ti and “light” Ca isotope effects measured in the studied refractory inclusions (see text).

(Huang et al., 2012) exhibit fractionated Ca isotopes with correspondingly little Ti isotope fractionation and dramatically lie off the theoretical Ca–Ti-condensation curve (Fig. 9).

The shallow (negative?) “trend” of the CAI data in Fig. 9 implies that Ti experienced limited fractionation in comparison to expectations from the large heavy isotope depletions observed in Ca. One explanation is that the Ti and Ca are inherited from distinct reservoirs, as the pervasive and sometimes variable  $^{50}\text{Ti}$  anomalies imply (Fig. 7, Table 1). In this case, the CAIs can be regarded as processed (e.g., melted) aggregates of pre-existing materials as opposed to condensates from a well-mixed gas. This hypothesis is supported by the textural relationships seen in Type A CAI EK5-2-1R (Fig. 1) that suggest localized partial resorption  $\pm$  overgrowth of refractory minerals, possibly indicating that coarse-grained inclusions grow in part by the consumption of earlier-formed refractory spinel-hibonite inclusions (SHIBs), a class of CAIs that often have large positive and negative  $^{50}\text{Ti}$  anomalies (e.g., Ireland, 1988, 1990; Kööp et al., 2016a, 2016b; Sahijpal et al., 2000). On the other hand, the measurements from a couple of the inclusions (major phases in EK5-2-1R and 461 B) do follow the theoretical fractionation model curve and thus can be explained by small ( $\leq 2^\circ\text{C}$ ) degrees of non-equilibrium condensation (i.e., undercooling).

Alternatively, the shallow slope defined by the data in Fig. 9 may indicate condensation from a well-mixed gas, but where Ca and Ti condensed in response to different degrees of undercooling (i.e.,  $S_{Ca} \neq S_{Ti}$ ). This is possible because in detail Ti has a higher  $T_{eq}$  than Ca by ~50 °C at their respective 50% condensation temperatures (at nebular pressures of  $10^{-5}$  bar, Fig. 10 (Ebel and Grossman, 2000)). In this case, a difference in undercooling of ~2 degrees is all that is required to produce these decoupled signatures (Figs. 8 and 11). The implication would be that the cooling rate during Ti condensation was slower than that when Ca condensed.

It can also be shown that the evidently uncorrelated Ca and Ti isotope records could be explained by a single condensation process, if the isotopic records reflect condensation of a localized ‘droplet’ and/or extremely fractionated nebular reservoir. This can be seen in Fig. 11 that shows the effects of instantaneous condensation where:

$$\delta = (\delta_0 + 1000)(\alpha_{\text{cond}} F^{\alpha_{\text{cond}}}) \quad (6)$$

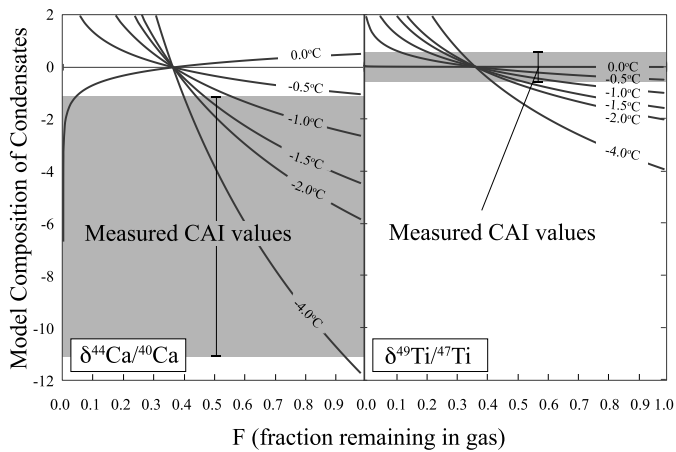


**Fig. 11.** Evolution of instantaneous isotopic composition of Ca and Ti during Rayleigh distillation. Ca and Ti isotopic signatures are typically enriched in heavy isotopes during non-equilibrium condensation (undercooling) until about  $F = 0.35$  and then become enriched in the light isotopes. At equilibrium, significant heavy Ca isotopic depletions can be produced after significant fractionation ( $F < 0.1$ ) (left).

We believe that models computed for instantaneous, rather than bulk condensation, are more representative of the processes dictating isotope fractionation recorded by the earliest formed condensates in the solar nebula. In general, all of the coarse-grained CAIs can be modeled by similar degrees of undercooling (e.g.,  $\sim 1$ – $2$  degrees) by instantaneous condensation. Likewise, the relatively extreme values measured in fine-grained CAI 3B3 can be explained by the endmember case of this scenario. The curves in Fig. 11 show that near-equilibrium condensation at more than  $\sim 95\%$  depletion of the gas reservoir in both Ca and Ti can explain the isotope ratios in both systems. If the model is taken at face value, i.e., the gaseous reservoir from which 3B3 condensed is the nebula and not an isolated portion of nebular gas, then fine-grained inclusions like 3B3 would have formed extremely late after  $>95\%$  of the Ca in the nebula had condensed. At thermodynamic equilibrium the temperature interval over which this would have occurred was  $\sim 1525$  to  $1450$  K (e.g., Ebel and Grossman, 2000). It is noteworthy that only about 5% or less of the Mg in the gas would have condensed through this temperature interval. Even if it condensed from a localized gas reservoir, this suggests that 3B3, a fine-grained CAI, actually represents a late or relatively late nebular condensation event and not condensation of a primordial solid. Future comparisons between additional measurements and these self-consistent theoretical models for Mg, Si, Ca, and Ti isotope ratios will allow us to more fully understand the effects of condensation and the formation history of these objects.

#### 5.4. Anomalous $^{50}\text{Ti}$ effects track reservoir mixing in the early Solar System

The existence and size of isotopic anomalies (e.g., Niederer and Papanastassiou, 1984) are typically thought to reflect a significant state of isotopic heterogeneity in the earliest Solar System, perhaps left over from molecular cloud heterogeneities on the grain scale (Young, 2016) or late stellar injection (e.g., Dauphas et al., 2010). The relative dilution of these isotopic anomalies has been used to track how less primitive solids and bulk planetary precursor materials were admixed and homogenized in the protoplanetary disk (Dauphas et al., 2014; Liu et al., 2009; Moynier et al., 2010a, 2010b; Simon et al., 2009; Trinquier et al., 2008).

A number of recent studies report  $^{50}\text{Ti}$  isotope anomalies in early formed solids (e.g., Leya et al., 2009; Kööp et al., 2016a, 2016b; Williams et al., 2016). The  $^{50}\text{Ti}$  effects measured in spinel-hibonite inclusions (i.e., SHIBs), platy hibonite crystals (PLACs),

and related hibonite-rich inclusions are extreme, ranging from large excesses to large depletions relative to the  $\sim 1\%$  level (i.e., 10  $\epsilon$ -units) effects typically reported for common Types A and B inclusions (e.g., Williams et al., 2016 and references therein), Fig. 7. Positive  $\epsilon^{50}\text{Ti}$  generally correlates with smaller Ni, Cr, and Zr isotopic anomalies as well as smaller Ca isotope anomalies. FUN inclusions are the exceptions as they usually exhibit strongly negative  $\epsilon^{50}\text{Ti}$  values (Niederer et al., 1985; Papanastassiou and Brigham, 1989; Loss et al., 1994; Williams et al., 2012, 2016).

Given the consistency between measured and modeled Ca and Ti isotope effects, a relatively simple non-equilibrium condensation scenario could explain 461 B. It likely condensed by  $\sim 1$ – $2$  degrees of undercooling from a rather primitive gas reservoir with  $\epsilon^{50}\text{Ti}$  excess. Its refractory isotopic signatures indicate that it did not later equilibrate in a planetary-like reservoir. In light of the textural and petrologic evidence that EK5-2-1R contains “exotic” refractory phases, it is interesting that the Ti laser spot analyses of EK5-2-1R that contain the greatest proportion of spinel-hibonite “mélange” on average exhibit the most “normal”  $\epsilon^{50}\text{Ti}$  value and normal mass dependent  $\delta^{49}\text{Ti}/^{47}\text{Ti}$ , whereas on average the spot analyses of EK5-2-1R dominated by major minerals exhibit a slightly higher  $\epsilon^{50}\text{Ti}$  value and more negative  $\delta^{49}\text{Ti}/^{47}\text{Ti}$  value, sharing a trend with 461 B (Fig. 9). The “relict” refractory minerals could actually have positive  $\delta^{49}\text{Ti}/^{47}\text{Ti}$  values, like 3B3, or possibly even higher, if one considers the fact that the range of spot analyses (see Figs. 4 and 7) all contain variable amounts of their coarse-grained host that exhibits negative  $\delta^{49}\text{Ti}/^{47}\text{Ti}$ . Nevertheless, they have mass dependent Ti isotope effects that appear decoupled from the Ca isotopic composition, whereas it appears that the melt that partially enveloped them recorded a signature of non-equilibrium condensation, as would be theoretically predicted by its corresponding Ca isotopic composition. In order for the apparent mass-dependent Ti isotopic heterogeneity of the CAI to have persisted, its history must either reflect: (1) condensation on the precursor mélange of refractory phases that was later partially remelted, and evolved as an open system isotopically, or (2) that the mélange of refractory precursors was enveloped/partially consumed by a protoCAI droplet of remelted condensates. In either scenario, a second reservoir is required to impart the  $\epsilon^{50}\text{Ti}$  excess observed in the host phase.

It is commonly assumed that the carriers of the neutron-rich anomalous isotope effects were added significantly before the now extinct  $^{26}\text{Al}$  ( $t_{1/2} = 0.7$  Ma) was added to the protosolar disk (Sahijpal and Goswami, 1998). An alternative explanation is that the concentrations of the neutron-rich isotopes and the  $^{26}\text{Al}$  in the early Solar System are averages inherited from the cloud material from which the Sun formed. In the latter scenario, canonical  $^{26}\text{Al}/^{27}\text{Al}_0$  represents the homogenization of grains with much lower and much higher  $^{26}\text{Al}/^{27}\text{Al}_0$  values that are averaged by processing in the solar protoplanetary disk (Young, 2016). EK-5-1R may represent a relatively primordial snapshot of this homogenization process in progress.

#### 5.5. Implications of intra-CAI calcium isotopic zoning

The *in-situ* evidence for Ca isotopic zoning across the interior of AL4884 reported here is a novel discovery and only measurable because of the combined developments in our micromilling and mass spectrometry techniques. Systematic stable isotope measurements across CAI margins have been performed for various elements on an individual element basis, but multiple complementary isotope profiles, such as for Ca together with Mg, have rarely been made for the same object (cf. Bullock et al., 2013; Knight et al., 2009; Shahar and Young, 2007). A previous hint of intra-CAI mass-dependent Ca isotopic heterogeneity exists in the early work of Niederer and Papanastassiou (1984) who reported resolvable effects among Al–Ti–pyroxene separates from a single

inclusion. The intra-CAI Ca isotopic zoning in AL4884 confirms that a refractory element can be isotopically fractionated at the scale of an inclusion. The systematic zoning profile (Fig. 6) implies that AL4884 condensed with isotopically light Ca compared to planetary materials and experienced later evaporation and/or a changing environment that significantly affected the Ca isotopic composition of its melilite mantle. The zoning could be due to a compositional change of the surrounding gas or could be related to changing conditions (e.g., less undercooling) that govern formation of the melilite mantle. It is unclear why zoning was not also observed in Crucible, or for that matter, how pervasive intra-CAI Ca isotopic zoning is among different CAIs. Yet, the more refractory nature of Ca and relative superposition of core and edge, respectively, suggest that the events that led to Ca isotopic zoning in AL4884 occurred prior to the history inferred by the isotopic signatures recorded by moderately volatile elements Mg and Si in CAIs and their Wark–Lovering rims (e.g., Simon et al., 2005).

Theoretical and experimental studies imply that evaporative residues must have been heated at low pressures for appreciable mass-dependent isotopic fractionation to be preserved (Davis et al., 1990; Nagahara and Ozawa, 2000; Yamada et al., 2006; Zhang et al., 2014). As such, the relatively heavy Ca isotope enrichment measured in the melilite margin of AL4884 and the heavy Mg isotope enrichments of many CAIs imply that they experienced evaporation at low pressures ( $<10^{-4}$  bar), conditions that are thought to be typical near the proto-Sun. It is noteworthy that little to no Mg could remain in the condensed phase at conditions hot enough to enrich heavy Ca by evaporation (Simon and DePaolo, 2010). Moreover, the normal Mg isotopic compositions reported in the margins and WL rims for several CAIs (Bullock et al., 2013; Simon et al., 2005) and for chondrules (Alexander et al., 2008; Galy et al., 2000) indicate that these materials formed from high local partial pressures and/or dust-rich regions of the solar nebula distinct from the hot inner solar nebula.

The recent comparison of isotopic data for CAIs (Niederer and Papanastassiou, 1984) and numerical models of Simon and DePaolo (2010) quantified the discrepancy between Ca and Mg isotope effects. The difference is likely due to their significantly different volatilities. As such, the measured Ca isotopic zoning profile of AL4884 indicate that analogous Mg isotopic zoning profiles likely reflect a later process(es), i.e., Simon and Young (2011). In fact, the sense of Ca isotopic zoning in AL4884 reported in this study is opposite that of its Mg isotopic zoning profile that decreases from “heavy” in the interior to relatively “normal” planetary values at the edge (Bullock et al., 2013). Later coeval condensation from a reservoir with distinct planetary-like Ca and Mg, related to formation of the melilite mantle of AL4884, could potentially explain the apparently converging profiles. But in such a scenario an additional solid-state diffusive exchange event that produces the isotopic zoning, of the type reported by Simon et al. (2005); Young et al. (2005), would also be required. Additionally, not all CAIs exhibit normal Mg isotope compositions at the edge, e.g., Simon and Young (2011) and the only other inclusion for which comparable *in-situ* Ca isotopic measurements are available, i.e., Crucible, appears homogeneous (this study). It follows that the sense of Ca zoning in AL4884 that is inconsistent with most reported Mg isotopic zoning profiles in CAIs that decrease from “heavy” in the interior to “normal” values at the edge implies that Mg isotopic signatures in CAIs in general may be susceptible to later modification in the solid-state, cf. MacPherson et al. (2012). Evidence for apparently conflicting Ca and Mg isotopic zoning profiles therefore opens up the possibility that similar Mg isotopic records measured in a number of other CAIs could also be related to a late isotopic exchange event. Although more corroborating evidence is required to confirm the interpretation for later isotopic exchange, the new

Ca data are difficult to reconcile with conventional interpretations for the canonical Al–Mg initial value of AL4884.

## 6. Conclusions

Here we report coordinated measurements of Ca and Ti isotopes in refractory inclusions. When compared to our latest condensation model calculations for isotopic fractionation it is clear that most, if not all, of the studied “normal” CAIs, and/or their precursor materials, record a multi-step/source condensation history. The extreme Ca and Ti isotope effects measured in the fine-grained CAI 3B3 exemplify the complicated condensation history of early formed solids. Such textures, that are often assumed to signify the primitive nature of nebular materials, may in fact reflect condensation from relatively evolved (i.e., fractionated) nebular gas rather than representing primordial condensates. The discovery of Ca isotopic zoning in Type B CAI AL4884 likely involves condensation from an evolving gaseous reservoir, presumably after  $^{26}\text{Al}$  was added to the Solar System, but before its moderately volatile element isotopic signatures were preserved. Thus, the existence of Ca isotopic zoning in AL4884 implies that its Mg isotope record pertains to a later, likely subsolidus, nebular history.

## Acknowledgements

The Department of Mineral Sciences, Smithsonian Institution is acknowledged for providing mineral standards. NASA Curation and CAPTEM are thanked for allocation of the lunar basalts used to evaluate the magnitude of stable Ca isotope effects among terrestrial bodies. Detailed and helpful comments of reviewers C. Williams and D. Papanastassiou and Editor F. Moynier are greatly appreciated. K. Ross, E. Berger, and K. McCain are thanked for technical assistance related to sample characterization by SEM. R. Mills and B. Ware are thanked for preparing a number of the reference materials for isotopic analysis, including the lunar basalts. NASA grants 11-COS11-0066 and 16-EW16\_2-0163 to J.I.S. and grant 14-EW14\_2-0060 to E.D.Y., and NSF grant EAR1530306 to E.A.S. supported this work.

## Appendix A. Supplementary material

Supplementary material related to this article can be found online at <http://dx.doi.org/10.1016/j.epsl.2017.05.002>.

## References

- Alexander, C.M.O., Grossman, J.N., Ebel, D.S., Ciesla, F.J., 2008. The formation conditions of chondrules and chondrites. *Science* 320, 1617–1619.
- Bullock, E.S., Knight, K.B., Richter, F.M., Kita, N.T., Ushikubo, T., MacPherson, G.J., Davis, A.M., Mendybaev, R.A., 2013. Mg and Si isotopic fractionation patterns in types B1 and B2 CAIs: implications for formation under different nebular conditions. *Meteorit. Planet. Sci.* 48, 1440–1458.
- Chen, H.-W., Lee, T., Lee, D.-C., Iizuka, Y., 2009. *In situ* Ti isotopic measurements by laser ablation MC-ICP-MS. *Terr. Atmos. Ocean. Sci.* 20, 703–712.
- Clayton, R.N., Mayeda, T.K., 1977. Correlated oxygen and magnesium isotope anomalies in Allende Inclusions. I: oxygen. *Geophys. Res. Lett.* 4, 295–298.
- Dauphas, N., Chen, J.H., Zhang, J., Papanastassiou, D.A., Davis, A.M., Travaglio, C., 2014. Calcium-48 isotopic anomalies in bulk chondrite and achondrites: evidence for a uniform isotopic reservoir in the inner protoplanetary disk. *Earth Planet. Sci. Lett.* 407, 96–108.
- Dauphas, N., Remusat, L., Chen, J.H., Roskosz, M., Papanastassiou, D.A., Stodolna, J., Guan, Y., Ma, C., Eiler, J.M., 2010. Neutron-rich chromium isotope anomalies in supernova nanoparticles. *Astrophys. J.* 720, 1577–1591.
- Davis, A.M., Hashimoto, A., Clayton, R.N., Mayeda, T.K., 1990. Isotope mass fractionation during evaporation of  $\text{Mg}_2\text{SiO}_4$ . *Nature* 347, 655–658.
- Ebel, D.S., Grossman, L., 2000. Condensation in dust-enriched systems. *Geochim. Cosmochim. Acta* 64, 339–366.
- Friedrich, J.M., Ebel, D.S., Weisberg, M.K., Birdsall, J., 2005. The Crucible: an unusual matrix-enclosing igneous CAI in NWA 2364 (CV3). In: *Lunar and Planetary Science Conference. Abst. # 1756*.

- Galy, A., Young, E.D., Ash, R.D., O'Nions, R.K., 2000. The formation of chondrules at high gas pressures in the solar nebula. *Science* 290, 1751–1753.
- Harper, C.L., Nyquist, L.E., Shih, C.Y., Wiesmann, H., 1990. Correlated  $^{96}\text{Zr}$ - $^{50,49,47}\text{Ti}$  Anomalies in Allende CAI: A New Constraint on the Origin of the Neutron-Rich Iron Peak e-Process Anomaly Suite. *Meteoritical Society*, p. 369.
- Huang, S., Farkaš, J., Yu, G., Petaev, M., Jacobsen, S.B., 2012. Calcium isotopic ratios and rare earth element abundances in refractory inclusions from the Allende CV3 chondrite. *Geochim. Cosmochim. Acta* 77, 252–265.
- Ireland, T.R., 1988. Correlated morphological, chemical, and isotopic characteristics of hibonites from the Murchison carbonaceous chondrite. *Geochim. Cosmochim. Acta* 52, 2827–2839.
- Ireland, T.R., 1990. Presolar isotopic and chemical signatures in hibonite-bearing refractory inclusions from the Murchison carbonaceous chondrite. *Geochim. Cosmochim. Acta* 54, 3219–3237.
- Jordan, M.K., Kohl, I.E., McCain, K.A., Simon, J.I., Young, E.D., 2017. Ti isotopes: echoes of grain-scale heterogeneity in the protoplanetary disk. In: 48th Lunar and Planetary Science Conference Abstr. 3032.
- Knight, K.B., Kita, N.T., Davis, A.M., Richter, F.M., Mendybaev, R.A., 2009. Mg and Si isotope fractionation within three Type B Ca–Al-rich inclusions. In: 40th Lunar and Planetary Science Conference Abstr. 2360.
- Kööp, L., Davis, A.M., Nakashima, D., Park, C., Krot, A.N., Nagashima, K., Tenner, T.J., Heck, P.R., Kita, N.T., 2016a. A link between oxygen, calcium and titanium isotopes in  $^{26}\text{Al}$ -poor hibonite-rich CAIs from Murchison and implications for the heterogeneity of dust reservoirs in the solar nebula. *Geochim. Cosmochim. Acta* 189, 70–95.
- Kööp, L., Nakashima, D., Heck, P.R., Kita, N.T., Tenner, T.J., Krot, A.N., Nagashima, K., Park, C., Davis, A.M., 2016b. New constraints on the relationship between  $^{26}\text{Al}$  and oxygen, calcium, and titanium isotopic variation in the early Solar System from a multielement isotopic study of spinel-bonite inclusions. *Geochim. Cosmochim. Acta* 184, 151–172.
- Leya, I., Schönbächler, M., Krähenbühl, U., Halliday, A.N., 2009. New titanium isotope data for Allende and Eremovka CAIs. *Astrophys. J.* 702, 1118–1126.
- Liu, M.C., McKeegan, K.D., Goswami, J.N., Marhas, K.K., Sahijpal, S., Ireland, T.R., Davis, A.M., 2009. Isotopic records in CM hibonites: implications for timescales of mixing of isotope reservoirs in the solar nebula. *Geochim. Cosmochim. Acta* 73, 5051–5079.
- Loss, R.D., Lugmair, G.W., Davis, A.M., MacPherson, G.J., 1994. Isotopically distinct reservoirs in the solar nebula: isotope anomalies in Vigarano meteorite inclusions. *Astrophys. J.* 436, L193–L196.
- MacPherson, G.J., Kita, N.T., Ushikubo, T., Bullock, E.S., Davis, A.M., 2012. Well-resolved variations in the formation ages for Ca–Al-rich inclusions in the early Solar System. *Earth Planet. Sci. Lett.* 331–332, 43–45.
- Millet, M.-A., Dauphas, N., Greber, N.D., Burton, K.W., Dale, C.W., Debret, B., MacPherson, C.G., Nowell, G.M., Williams, H.M., 2016. Titanium stable isotope investigation of magmatic processes on the Earth and Moon. *Earth Planet. Sci. Lett.* 449, 197–205.
- Moynier, F., Simon, J.I., Podosek, F.A., Meyer, B.S., Brannon, J., DePaolo, D.J., 2010a. Ca isotope effects in Orgueil leachates and the implications for the carrier phases of  $^{54}\text{Cr}$  anomalies. *Astrophys. J.* L7–L13.
- Moynier, F., Agranier, A., Hezel, D.C., Bouvier, A., 2010b. Sr stable isotope composition of Earth, the Moon, Mars, Vesta and meteorites. *Earth Planet. Sci. Lett.* 300, 359–366.
- Moynier, F., Bouvier, A., Blichert-Toft, J., Telouk, P., Gasperini, D., Albarede, F., 2006. Europium isotopic variations in Allende CAIs and the nature of mass-dependent fractionation in the solar nebula. *Geochim. Cosmochim. Acta* 70, 4287–4294.
- Moynier, F., Pringle, E.A., Bouvier, A., Moureau, J., 2015. Barium stable isotope composition of the Earth, meteorites, and calcium–aluminum-rich inclusions. *Chem. Geol.* 413, 1–6.
- Nagahara, H., Ozawa, K., 2000. Isotopic fractionation as a probe of heating processes in the solar nebula. *Chem. Geol.* 169, 45–68.
- Niederer, F.R., Papanastassiou, D.A., Wasserburg, G.J., 1980. Endemic isotopic anomalies in titanium. *Astrophys. J.* 240, L73–L77.
- Niederer, F.R., Papanastassiou, D.A., Wasserburg, G.J., 1981. The isotopic composition of titanium in the Allende and Leoville meteorites. *Geochim. Cosmochim. Acta* 45, 1017–1031.
- Niederer, F.R., Papanastassiou, D.A., 1984. Ca isotopes in refractory inclusions. *Geochim. Cosmochim. Acta* 48, 1279–1293.
- Niederer, F.R., Papanastassiou, D.A., Wasserburg, G.J., 1985. Absolute isotopic abundances of Ti in meteorites. *Geochim. Cosmochim. Acta* 49, 835–851.
- Niemeyer, S., 1988. Titanium isotopic anomalies in chondrules from carbonaceous chondrites. *Geochim. Cosmochim. Acta* 52, 309–318.
- Papanastassiou, D.A., Brigham, C.A., 1989. The identification of meteorite inclusions with isotope anomalies. *Astrophys. J. Lett.* 338, L37–L40.
- Petaev, M., Jacobsen, B., 2009. Petrologic study of S101, a new forsterite-bearing CAI from the Allende CV3 chondrite. *Geochim. Cosmochim. Acta*, 5100–5114.
- Richter, F.M., Davis, A.M., Ebel, D.S., Hashimoto, A., 2002. Elemental and isotopic fractionation of Type B calcium-, aluminum-rich inclusions: experiments, theoretical considerations, and constraints on their thermal evolution. *Geochim. Cosmochim. Acta* 66, 521–540.
- Russell, W.A., Papanastassiou, D.A., Tombrello, T.A., 1978. Ca isotope fractionation on earth and other solar-system materials. *Geochim. Cosmochim. Acta* 42, 1075–1090.
- Sahijpal, S., Goswami, J.N., 1998. Refractory phases in primitive meteorites devoid of  $^{26}\text{Al}$  and  $^{41}\text{Ca}$ : representative of samples of first solar system solids? *Astrophys. J.* 509, L137–L140.
- Sahijpal, S., Goswami, J.N., Davis, A.M., 2000. K, Mg, Ti, and Ca isotopic compositions and refractory trace element abundances in hibonites from CM and CV meteorites: implications for early solar system processes. *Geochim. Cosmochim. Acta*, 1989–2005.
- Schauble, E.A., 2011. First-principles estimates of equilibrium magnesium isotope fractionation in silicate, oxide, carbonate and hexaquaamagnesium ( $2^+$ ) crystals. *Geochim. Cosmochim. Acta* 75, 844–869.
- Shiller, M., Paton, C., Bizzarro, M., 2015. Evidence for nucleosynthetic enrichment of the protosolar molecular cloud core by multiple supernova events. *Geochim. Cosmochim. Acta* 149, 88–102.
- Shahar, A., Young, E.D., 2007. Astrophysics of CAI formation as revealed by silicon isotope LA-MC-ICPMS of an igneous CAI. *Earth Planet. Sci. Lett.* 257, 497–510.
- Simon, J.I., DePaolo, D.J., 2010. Stable calcium isotopic composition of meteorites and rocky planets. *Earth Planet. Sci. Lett.* 289, 457–466.
- Simon, J.I., DePaolo, D.J., Moynier, F., 2009. Calcium isotope composition of meteorites, Earth, and Mars. *Astrophys. J.* 702, 707–715.
- Simon, J.I., Young, E.D., 2011. Resetting, errorchrons and the meaning of canonical CAI initial  $^{26}\text{Al}/^{27}\text{Al}$  values. *Earth Planet. Sci. Lett.* 304, 468–482.
- Simon, J.I., Young, E.D., Russell, S.S., Tonui, E.K., Dyl, K.A., Manning, C.E., 2005. A short timescale for changing oxygen fugacity in the solar nebula revealed by high-resolution Al-26-Mg-26 dating of CAI rims. *Earth Planet. Sci. Lett.* 238, 272–283.
- Trinquier, A., Bizzarro, M., Ulfbeck, D., Elliott, T., Coath, C.D., Mendybaev, R.A., Richter, F.M., Krot, A.N., 2008. Origin of Ti isotope heterogeneity in the protoplanetary disk. *Geochim. Cosmochim. Acta* 72, A956.
- Trinquier, A., Elliott, T., Ulfbeck, D., Coath, C.D., Krot, A.N., Bizzarro, M., 2009. Origin of nucleosynthetic isotope heterogeneity in the solar protoplanetary disk. *Science* 324, 374–376.
- Uyeda, C., Tsuchiyama, A., Okano, J., 1991. Magnesium isotopic fractionation of silicates produced in condensation experiments. *Earth Planet. Sci. Lett.* 107, 138–147.
- Valdes, M.C., Moreira, M., Foriel, J., Moynier, F., 2014. The nature of Earth's building blocks as revealed by calcium isotopes. *Earth Planet. Sci. Lett.* 394, 135–145.
- Wasserburg, G.J., Lee, T., Papanastassiou, D.A., 1977. Correlated O and Mg isotopic anomalies in Allende inclusions: II magnesium. *Geophys. Res. Lett.* 4, 299–302.
- Wark, D.A., Lovering, J.F., 1977. Marker events in the early evolution of the solar system: evidence from rims on Ca–Al-rich inclusions in carbonaceous chondrites. In: *Proceedings of Lunar Science Conference 8th*, pp. 95–112.
- Williams, C.D., Janney, P.E., Hines, R.R., Wadhwa, M., 2016. Precise titanium isotope compositions of refractory inclusions in the Allende CV3 chondrite by LA-MC-ICPMS. *Chem. Geol.* 436, 1–10.
- Williams, C.D., Wadhwa, M., Janney, P.E., Hines, R.R., Bullock, E.S., MacPherson, G.J., 2012. Ti, Si and Mg isotope systematics of FUN CAI CMS-1. In: 75th Annual Meeting of the Meteoritical Society, Abstr. # 5102.
- Yamada, M., Tachibana, S., Nagahara, H., Ozawa, K., 2006. Anisotropy of Mg isotopic fractionation during evaporation and Mg self-diffusion of forsterite in vacuum. *Planet. Space Sci.* 54, 1096–1106.
- Young, E.D., 2016. Bayes' theorem and early solar short-lived radionuclides: the case for an unexceptional origin for the solar system. *Astrophys. J.* 826, 129. 6 pp.
- Young, E.D., Galy, A., Nagahara, H., 2002. Kinetic and equilibrium mass-dependent isotope fractionation laws in nature and their geochemical and cosmochemical significance. *Geochim. Cosmochim. Acta* 66, 1095–1104.
- Young, E.D., Nagahara, H., Mysen, B.O., Audet, D.M., 1998. Non-Rayleigh oxygen isotope fractionation by mineral evaporation: theory and experiments in the system  $\text{SiO}_2$ . *Geochim. Cosmochim. Acta* 62, 3109–3116.
- Young, E.D., Simon, J.I., Galy, A., Russell, S.S., Tonui, E., Lovera, O., 2005. Supracanonical Al-26/Al-27 and the residence time of CAIs in the solar protoplanetary disk. *Science* 308, 223–227.
- Zhang, J., Dauphas, N., Davis, A.M., Leya, I., Fedkin, A., 2012. The proto-Earth as a significant source of lunar material. *Nat. Geosci.* 5, 251–255.
- Zhang, J., Dauphas, N., Davis, A.M., Pourmand, A., 2011. A new method of MC-ICPMS measurement of titanium isotopic composition: identification of correlated isotope anomalies in meteorites. *J. Anal. At. Spectrom.* 26, 2197–2205.
- Zhang, J., Huang, S., Davis, A.M., Dauphas, N., Hashimoto, A., Jacobsen, S.B., 2014. Calcium and titanium isotopic fractionations during evaporation. *Geochim. Cosmochim. Acta* 140, 365–380.
- Zhu, X.K., Makishima, A., Guo, Y., Belshaw, N.S., O'Nions, R.K., 2002. High precision measurement of titanium isotope ratios by plasma source mass spectrometry. *Int. J. Mass Spectrom.* 220, 21–29.